ACS OMEGA

http://pubs.acs.org/journal/acsodf

Article

Grape Seed Extract Assisted Synthesis of Dual-Functional Anatase TiO_2 Decorated Reduced Graphene Oxide Composite for Supercapacitor Electrode Material and Visible Light Photocatalytic Degradation of Bromophenol Blue Dye

Subramanian Ramanathan, Sasikumar Moorthy, Subramaniyan Ramasundaram, Hari Krishna Rajan, Sujayakumar Vishwanath, SteplinPaulSelvin Selvinsimpson, Arulappan Durairaj, Byungki Kim, and Samuel Vasanthkumar*

Cite This: *ACS Omega* 2021, 6, 14734−14747

Read Online

ACCESS | Metrics & More | Article Recommendations | Supporting Information

ABSTRACT: The grape extract is a potential natural reducing agent because of its high phenolic content. The extracts of seeds, skin, and pulp of grape were prepared by digestion, grinding, and soxhlet methods and used for reducing graphene oxide (GO). The reduced GO made using the soxhlet extract of grape seed (GRGO) was hydrothermally treated with titanium dioxide (TiO_2) for the synthesis of GRGO−TiO_2 nanocomposite. The X-ray diffraction (XRD), thermogravimetric analysis (TGA), Fourier transform infrared (FT-IR), UV−vis, photoluminescence, and Raman spectra studies further confirmed the formation of GRGO and the GRGO−TiO_2 hybrid. Scanning electron microscope and transmission electron microscope studies showed the decoration of spherical TiO_2 particles (<100 nm) on the few-layered GRGO sheets. The GRGO−TiO_2 hybrid was explored as a working electrode for supercapacitors and visible light photocatalyst for water decontamination. GRGO−TiO_2 showed higher specific capacitance (175 F g^{-1}) than GRGO (150 F g^{-1}) and TiO_2 (125 F g^{-1}) in an aqueous electrolyte. GRGO−TiO_2 exhibited 83.6% capacitance retention even after 2000 cycles, indicating the good stability of the material. Further, under visible light irradiation (λ > 400 nm), GRGO−TiO_2 showed ∼30% higher photo-oxidation of the bromophenol blue (BPB) dye than TiO_2. Also, GRGO−TiO_2 decreased the total organic carbon content of BPB from 92 to 18 ppm. Overall, the soxhlet extract of grape seed was found to be a cost-effective reducing agent for the preparation of GRGO, which is a suitable material to be used in supercapacitors and photocatalysis.

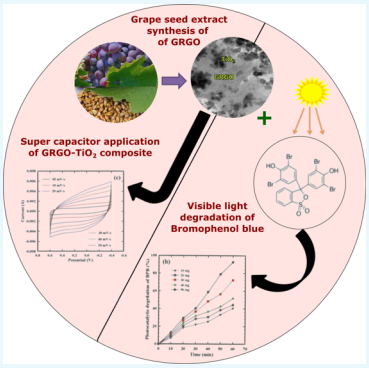

1. INTRODUCTION

An atom-thick two-dimensional all-carbon chemical structure makes graphene a material possessing greater electronic conductivity, mechanical strength, and thermal stability.[1] To produce in a large scale, graphene sheets stacked in graphite are being subjected to oxidative chemical exfoliation, which introduces oxygen functionalities in the edges and surfaces and renders nonconducting graphene oxide (GO) sheets.[2,3] For applications demanding electronic conductivity, such as electrodes in electronic circuits and supercapacitors, the original all-carbon chemical structure of graphene sheets must be restored. To achieve structural restoration, the oxygen functionalities in GO sheets are often removed by either liquid-phase or solid-state reduction.[4] Heating of GO to elevated temperatures is required to achieve solid-state reduction that often leads to restacking of graphene sheets. Classical chemical reducing agents, microorganisms, and phytoextracts have been used as liquid-phase reducing agents.[5−7] Due to their strong reducing power, the classical chemical reducing agents such as hydrazine and sodium borohydride were causing irreversible aggregation of graphene sheets upon reduction. Irreversible aggregation restricts the application of reduced GO (RGO) sheets via cost-effective solution processing. In addition, these reducing agents are highly toxic and expensive.[8,9] Clean and aseptic conditions must be maintained to culture and grow the microorganism, so the microbial reduction of GO is considered as cumbersome.[10,11]

Natural and plant extracts can be processed at ambient environment, and their use eliminates the chemical toxicity. Notably, their mild reducing potential allows the slow and controlled reduction of GO, and thereby, the problems of restacking and irreversible aggregation can be avoided. Extracts

Received: November 9, 2020
Accepted: February 12, 2021
Published: May 29, 2021

of orange peel,[12] lemon,[13] barberry fruit,[14] guava leaf,[15] and carrot[16] are typical phytoextracts investigated for this purpose. Similarly, grape extract is a rich source of phytochemicals such as polyphenols, flavonoids, and catechins.[17] Grape fruit has three parts: the pulp, skin, and seed. The total extractable phenolics in grape are about 10% in pulp, 60−70% in the seeds, and 28−35% in the skin.[18] Due to these polyphenol constituents, grape extract reduces noble metal salts, ketones, and nitro compounds. Grape extract was explored for the synthesis of gold and silver nanoparticles.[19] Therefore, to take advantage of its great reducing ability, it was used as a reducing agent for the reduction of GO into RGO.

The RGO materials prepared by chemical and thermal reduction have found applications in electronics, energy, environment, and biological fields.[20−24] Accordingly, the suitability of RGO prepared using grape extract can also be evaluated for typical applications. Exploring representative applications in the fields of energy and environment would be beneficial as the world needs to address the increase in demand for energy and rise in the issue of water pollution associated with chemical contamination. Supercapacitors are an electrochemical energy storage system that can store more energy than a conventional capacitor. In combination with transition metal oxides (TMOs), RGO has been used to prepare supercapacitors with high energy and power densities.[25] Semiconductor photocatalysis is considered as an environmentally benign technology for the mineralization of organic contaminants in water.[3,26,27] Similar to supercapacitors, RGO is incorporated with TMOs to obtain a visible light active photocatalyst as well as for improving the efficiency under ultraviolet light. It is very important to emphasize that TiO_2 is a one of the most efficient TMOs that has found use in both supercapacitor and photocatalysis applications.[28,29] Thus, preparation of grape extract reduced graphene oxide (GRGO) and its TiO_2 hybrids (GRGO−TiO_2) can be a useful application-oriented strategy. To obtain an efficient GRGO−TiO_2 useful for the aforementioned applications, the reducing capability of various parts of grape fruit must be evaluated systematically such as by using various extraction methods; to the best of knowledge, so far, there has been no attempt made.

In the present investigation, three different parts of grape fruit, i.e., the pulp, seed, and skin, were separated, and their aqueous extracts were made through digestion, grinding, and soxhlet methods. To evaluate the chemical constituents, these extracts were subjected to gas chromatograph equipped mass spectrometer (GCMS) analysis and used for reducing GO. The resultant grape extract reduced GO (GRGO) was hydrothermally treated with titanium alkoxide. The chemical compositions of GO, GRGO, and GRGO−TiO_2 were studied using ultraviolet−visible (UV−vis), Fourier transform infrared (FTIR), Raman, X-ray photoelectron (XPS), and energy-dispersive X-ray (EDS) spectroscopic analyses. Crystalline structures of these materials were evaluated by X-ray diffraction, and field-emission scanning electron microscope (Fe-SEM) and transmission electron microscope (TEM) were used to observe the morphology. To explore the supercapacitor application, the working electrode fabricated by coating the GRGO−TiO_2 hybrid on a graphite sheet was characterized using an electrochemical workstation. Further, GRGO−TiO_2 was explored for the photocatalytic degradation of bromophenol blue (BPB) dye under visible light irradiation.

2. EXPERIMENTAL

Graphite flakes (CAS No. 7782-42-5 (60 mesh)), sulfuric acid (H_2SO_4) with 0.1 M concentration (CAS No. 7664-93-9), hydrochloric acid (HCl) with 0.1 M concentration (7647-01-0), hydrogen peroxide (H_2O_2) (7722-84-1), potassium permanganate ($KMnO_4$) (7722-64-7), sodium nitrate ($NaNO_3$) (7631-99-4), and tetrabutyltitanate (5593-70-4) were purchased from Sigma Aldrich (India) and used as received. Acetylene black (1333-86-4), polyvinylidene fluoride (24937-79-9), and *N*-methyl-2-pyrrolidone (872-50-4) were purchased from Sigma Aldrich. Waste black grapes (*Vitis vinifera*) were collected from the Alanduari fruit market (near Karunya Institute of Technology and Sciences), Coimbatore, Tamil Nadu, India.

2.1. Preparation of GRGO and GRGO−TiO_2. The scheme shown in Figure 1 depicts the various steps involved in the preparation of GRGO and GRGO−TiO_2.

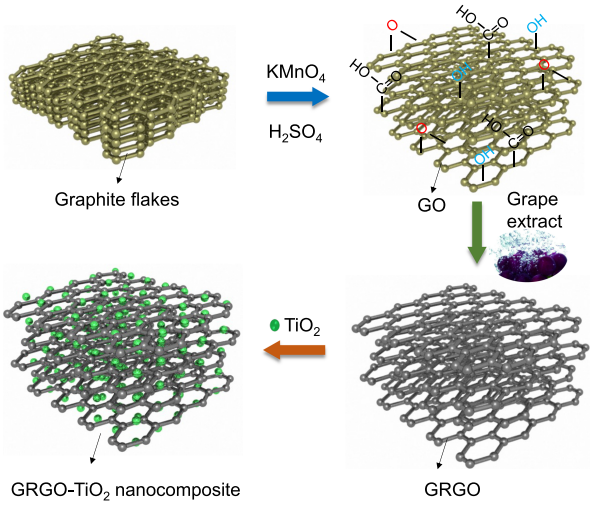

Figure 1. Schematic of the synthesis of GRGO and GRGO−TiO_2.

2.1.1. Synthesis of GO. The scheme shown in Figure 1 depicts the various steps involved in the preparation of the GRGO−TiO_2 hybrid. Graphite oxide was synthesized by the modified Hummer's method.[2] Under ice-cold conditions, 2 g of graphite flakes was stirred with 60 mL of H_2SO_4, and 6 g of $KMnO_4$ was added gradually added. Once $KMnO_4$ addition was made, the system was brought to 35 °C and the stirring was further continued for the next 48 h. To the resultant pasty brown crude mixture, 1 L of deionized (D.I.) water was added. Then, 10 mL of H_2O_2 was gradually added to terminate the oxidation reaction. The solid residue was washed with 0.3 M HCl and D.I. water. Finally, graphite oxide powder was obtained after drying the washed solid residue at 60 °C under vacuum.

2.1.2. Preparation of Black Grape Fruit Extract from Three Different Parts by Three Different Extraction Methods. First, the pulp, seed, and skin parts of black grape fruit (contains lots of resveratrol, a phytochemical and antioxidant) were separated and subjected to boiling water digestion, grinding, and soxhlet extraction. In all the methods, these parts were processed with 100 mL of D.I. water. For water digestion, these parts were separately treated at 100 °C for 3 h and filtered. A kitchen grinder was used for grinding. The grounded contents digested in water were filtered with a 70 mesh streel filter. Soxhlet extraction was performed with D.I. water at

https://dx.doi.org/10.1021/acsomega.0c02325
ACS Omega 2021, 6, 14734−14747

refluxing conditions. The contents from both of these methods were made up to 150 mL using D.I. water and used for the preparation of GRGO.

2.1.3. Synthesis of GRGO by Grape Extract. For the synthesis of GRGO, 50 mg of graphite oxide powder was exfoliated into GO by sonicating with 100 mL of ethanol for 1 h. In separate experiments, 30 mL of grape extract mentioned in Section 3.2 was mixed with GO−ethanol dispersion and refluxed at 80 °C for 5 h. After reduction, the brown GO dispersion turned black, and it was centrifuged at 10,000 rpm for 20 min. The residue was washed with water and dried at ambient temperatures under vacuum overnight. As-obtained GRGO was collected for further use.

2.1.4. Synthesis of the GRGO−TiO_2 Nanocomposite. GRGO powder (200 mg) was dispersed with 60 mL of ethanol by sonication for 3 h, the resultant GRGO dispersion was centrifuged at 5000 rpm for 10 min, and the supernatant was collected. Then, the reaction mixture containing 5 mL of GRGO dispersion and 10 mL of tetrabutyltitanate solution was added to 0.1 mL of the HF solution of cooled condition under vigorous stirring. After stirring for 2 h at room temperature, the black solution was transferred into a 100 mL Teflon-lined stainless steel autoclave for hydrothermal reaction, heated at 200 °C for 24 h, and centrifuged at 10,000 rpm for 15 min. The final product was dried at ambient temperatures under vacuum for 24 h. The GRGO−TiO_2 nanocomposite was synthesized where both anatase and rutile phases of titania were present. After completing the reaction, the final product was filtered. To remove impurities from the product, it was washed with a copious amount of DD and acid. In addition, the final product was dried at 70 °C in a hot air oven overnight to get the black fine carbon powder by grinding. Meanwhile, bare titanium dioxide (TiO_2) (without GRGO) for comparison was synthesized following a similar procedure.

2.1.5. Fabrication of Electrodes for Supercapacitor. The GRGO, TiO_2, and GRGO−TiO_2 electrodes were prepared using the binder mixture prepared as below. In the weight ratio of 80:10:10, acetylene black and the binder polyvinylidene fluoride were dispersed in *N*-methyl-2-pyrrolidone. The resultant slurry was mixed with GRGO, TiO_2, or GRGO−TiO_2 and uniformly coated onto a graphite sheet (1×1 cm^2) and dried at 50 °C for 12 h in air. The electrochemical cell was a three-electrode system, where Pt wire; Ag/AgCl, KCl (saturated); and the hybrid or reference material coated graphite sheet were used as counter electrode, reference electrode, and working electrode, respectively. A 6 M KOH aqueous solution was used as the electrolyte. The electrochemical tests were performed at ambient temperature. The cyclic voltammetry (CV) was carried out at scan rate of 5 to 50 mV s^{-1}, and the voltage range was −0.4 to 0.6 V.

2.2. Characterization. FTIR spectra were recorded using a Shimadzu FT-IR spectrometer (Japan). UV−Vis spectra were measured using a JASCO V-630 (Japan) instrument. XRD patterns were obtained using a Shimadzu XRD 6000 (Japan). TEM (JEM 2100) and FE-SEM images were observed with JEM 2100 and JOEL JSM-6390 instruments, respectively. TGA was performed with a Shimadzu DTG-60 device (Japan). GC−MS studies were carried out using a Shimadzu GC−MS-QP2010 Ultra instrument.

2.3. Photocatalytic Experiment. The photocatalytic action of GRGO−TiO_2 was assessed by examining the photodegradation of the BPB dye as a model contamination under visible light illumination. For this study, a 70 W CFL light (λ < 400 nm, 70 WBCB22 220−240 V, Philips India) was used. In this experiment, 10−50 mg of GRGO−TiO_2 was suspended in 100 mL of the aqueous BPB solution (1×10^{-5} M) in a hollow vessel and equilibrated in the dark for 10 min with constant stirring. After being exposed to the light source, for every 10 min, 3 mL aliquots were withdrawn. Using a UV−Visible spectrophotometer, the concentration of BPB was monitored on the basis of changes in its absorbance at 590 nm. The extent of photo-oxidation of BPB was determined by using eq 1:

$$\%D = (A_0 - A_t) \times 100/A_0 \quad (1)$$

where A_0 and A_t are the initial and equilibrium concentration at time "t", respectively.

3. RESULTS AND DISCUSSION

3.1. Evaluation of the Reducing Capability of Various Grape Extracts. First, the capability of grape extracts to reduce the GO was evaluated using XRD studies (Figure 2).

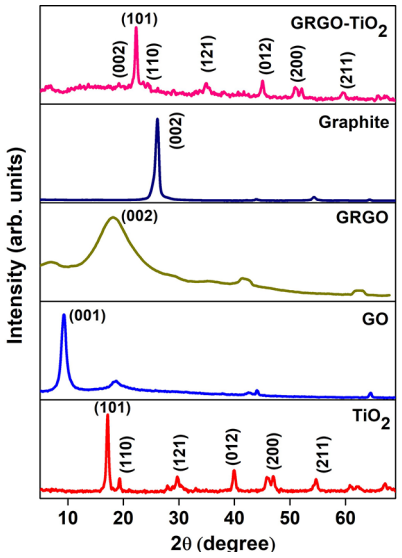

Figure 2. XRD patterns of graphite, GO, GRGO, TiO_2, and GRGO−TiO_2 nanocomposites.

The changes in the intensity of 2θ peaks 10.5 and 26.35° were taken into account. The former is associated with graphite oxide that arises due to the increase in the interlayer spacing to 0.34 nm, and the latter corresponds to graphite. Among all samples, GRGO prepared using the soxhlet extract of grape seed showed relatively sharp and intense peak graphitic at 2θ = 20.35°. In addition to that, the 10.5° observed in graphite oxide almost completely disappeared, confirming the restoration of the graphitic structure. Thus, the SES extract was found to be a more efficient reducing agent (Figure 3). TGA results (Figure 4) further confirmed the deoxygenation of GO by SES. Both GO and GRGO showed two stages of weight loss. In the first stage, up to 200 °C, the residual water and oxygen functionalities such as hydroxyl, epoxy, and carboxyl groups were removed. This was less prominent in GRGO because its hydrophobicity, caused by the deoxygenation, occurred during reduction with SES. In stage two, above 200 °C, the pyrolysis led to the breakage of carbon bonds. At around 550 °C, the bonded carbon turned to residue. The GRGO shows more

https://dx.doi.org/10.1021/acsomega.0c02325
ACS Omega 2021, 6, 14734−14747

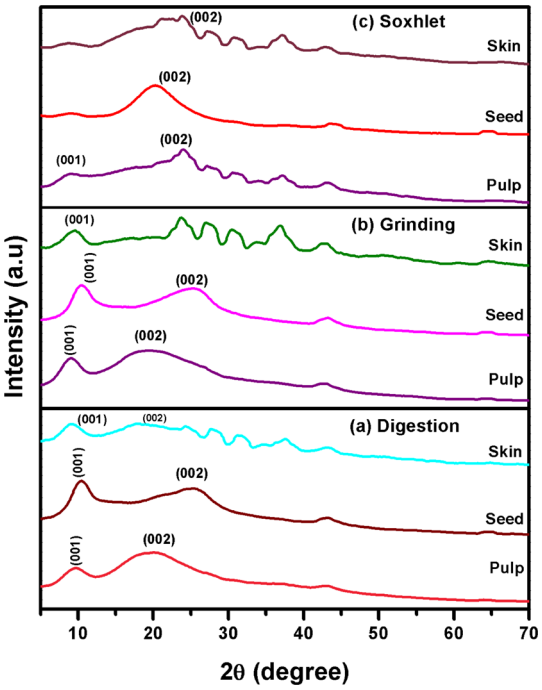

Figure 3. XRD patterns of (a) digestion method extract (seed, flesh, and skin) rGO, (b) grinding method extract (seed, flesh, and skin) rGO, and (c) soxhlet method extract (seed, flesh, and skin) rGO.

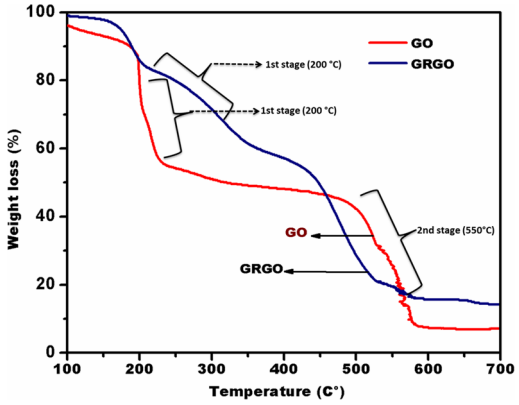

Figure 4. TGA thermograms of GO and GRGO prepared using the soxhlet extract of grape seed (SES).

residue than graphite oxide due to its high carbon content. These results confirmed the formation of GRGO.

To obtain an insight regarding the mechanism involved in the reduction of GO, SES was subjected to GC−MS analysis. The GC−MS spectra are shown in Figure S1. The molecular ion peak seen at 789 m/z was found, which was identified as echinacoside (a phenolic compound). The other peaks are also relevant to phenolic compounds. The higher concentration of these phenolic compounds accounted for the higher reducing capability of SES. Figure 5 shows the plausible mechanism for the reduction of GO by the phenolic compounds. The removal of oxygen from GO is initiated by the removal of epoxide groups from GO. The epoxide removal follows an SN_2 mechanism in which hydrogen in the polyphenol group attacks the sp^2 carbon atom of the epoxide ring and opens it. It leads to the formation of the C−O−C bond between GO and polyphenol in intermediate I. In step two, another hydrogen atom from the polyphenol is transferred into the hydroxyl

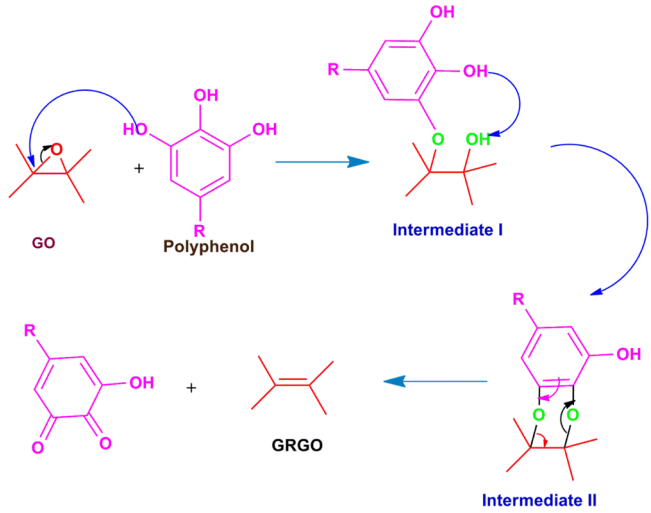

Figure 5. Plausible mechanism for the reduction of GO by phenolic compounds in SES.

group of GO and forms the C−O−C bond in intermediate II. Finally, the reduced form of GO is formed. Likewise, the carboxylic acid group undergoes a condensation reaction during reduction to form ester, and finally, the reduction causes the ring opening in the ester groups to form the reduced graphene oxide.[30,31]

3.2. Preparation and Physiochemical Properties of GRGO−TiO_2 Hybrids. By considering the highest efficiency in terms of reducing GO, the SES reduced GO was used for preparing GRGO−TiO_2 hybrids. Unless otherwise stated, the GRGO discussed hereafter was prepared using SES. UV−Vis spectra of GO and GRGO are shown in Figure 6. In GO, UV absorption peaks appeared at 232, which corresponds to the $\pi-\pi^*$ transitions of aromatic C═C bonds, and the shoulder 305 nm is attributed to the $n-\pi^*$ transition of aromatic C═O bonds. Figure 7a,b shows the UV−Vis spectra of TiO_2 and GRGO−TiO_2. GRGO shows a red shift at 278 nm due to the restoration of electronic conjugation during the reduction process. Because of the reduction mechanism, all the oxygen functional groups are removed by natural reducing agents such as the seed part of grape; at the same time, the C═C double bonds were restored, and therefore, it enhanced the conjugation of π bonds.TiO_2 exhibited the peak relevant to its anatase phase at 303 nm. The peaks associated with GRGO and TiO_2 were found in GRGO−TiO_2. Due to the intermolecular interactions between GRGO and TiO_2, the peak associated with TiO_2 was red shifted to 344 nm. Notably, GRGO−TiO_2 showed absorption beyond 400 nm, which indicates its ability to absorb visible light. The Tauc plot (Figure 7c,d) was used to calculate the band gap of TiO_2 and GRGO−TiO_2. The band gap of TiO_2 appeared to be 3.68 eV, which corresponds to the energy of the UV region. The GRGO−TiO_2 hybrid exhibited the band gap of 2.89 eV, confirming its absorption of visible light. Thus, GRGO imparted the visible light activity to TiO_2.The PL emission spectra of TiO_2 and GRGO−TiO_2 are shown Figure 8. TiO_2 exhibited the intense bands at 450 and 500 nm, while in the same range, a broad band was observed for GRGO−TiO_2. Due to the addition of GRGO to the intensity of peaks associated with TiO_2 was decreased because of the suppression of the electron−hole recombination. Lowering of the electron−hole

https://dx.doi.org/10.1021/acsomega.0c02325
ACS Omega 2021, 6, 14734−14747

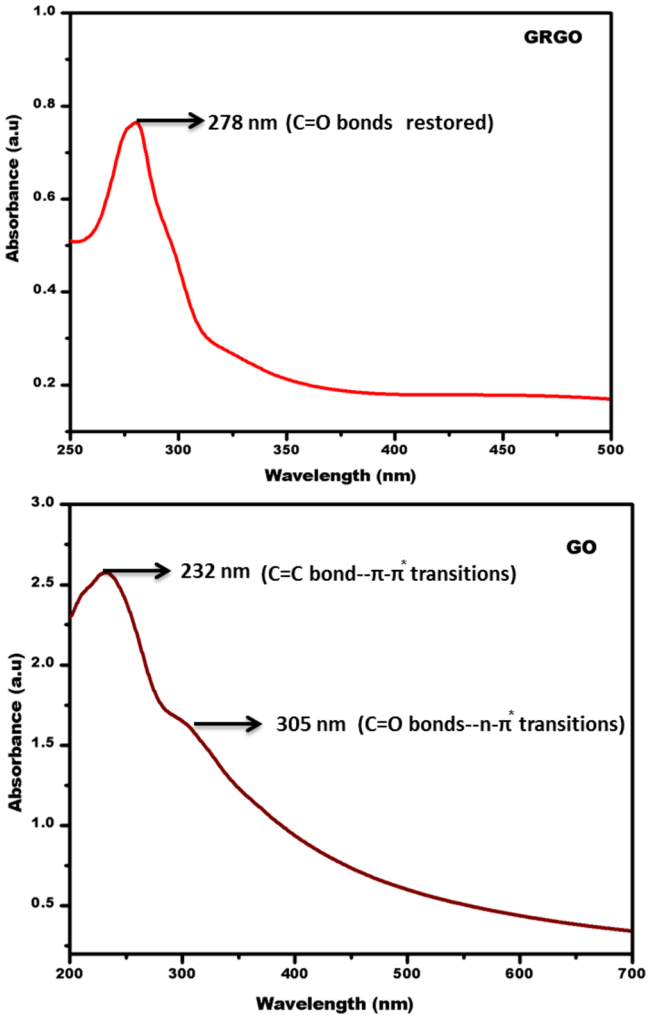

Figure 6. UV−Vis spectra of GO and GRGO.

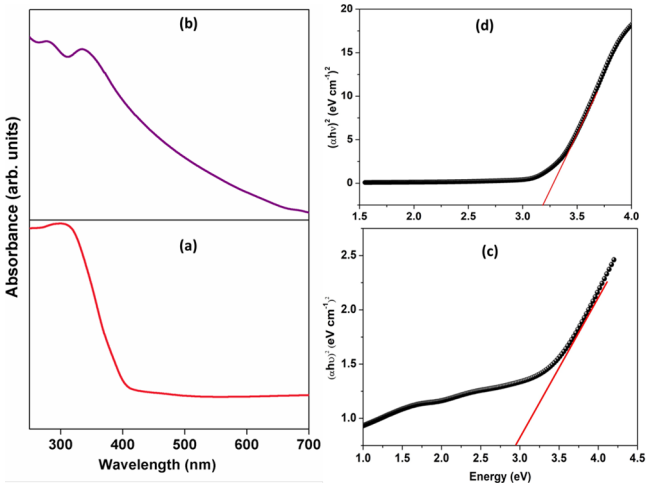

Figure 7. UV−vis spectra of (a) TiO_2 and (b) GRGO−TiO_2. (c) Tauc plot of TiO_2 and (d) GRGO−TiO_2.

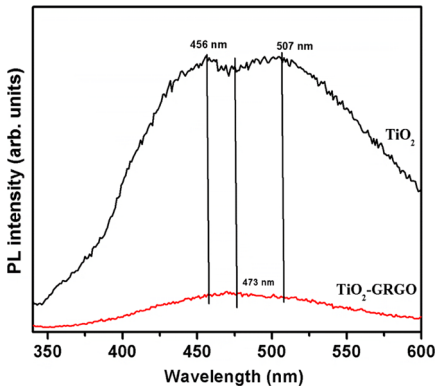

Figure 8. Photoluminescence (PL) spectra of TiO_2 and GRGO−TiO_2.

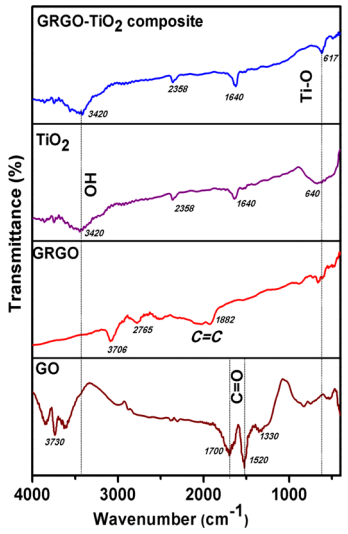

Figure 9. FTIR spectra of graphite, GO, rGO, TiO_2, and rGO−TiO_2 composites.

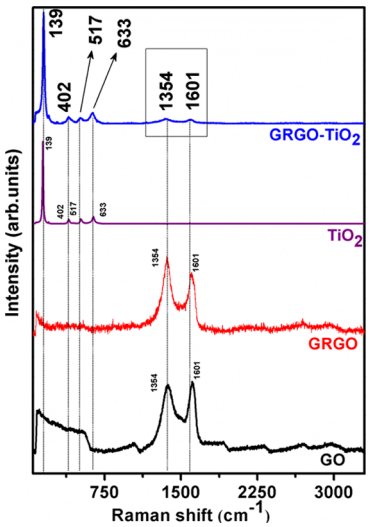

Figure 10. Raman spectrum of GO, GRGO, TiO_2, and GRGO−TiO_2 nanocomposites.

recombination increases the availability of electron and holes for photocatalytic reactions.

Figures 2, 9, and 10 show the XRD patterns, FTIR, and Raman spectra of GO, GRGO, TiO_2, and GRGO−TiO_2. In the XRD patterns, graphitic oxide exhibited the peaks associated with oxidized and undisturbed graphitic carbon peaks at 10.5 and 26.35°, respectively. Hydrothermally synthesized TiO_2 was found to be crystallized into both anatase and rutile phases. The former appeared predominant as

https://dx.doi.org/10.1021/acsomega.0c02325
ACS Omega 2021, 6, 14734−14747

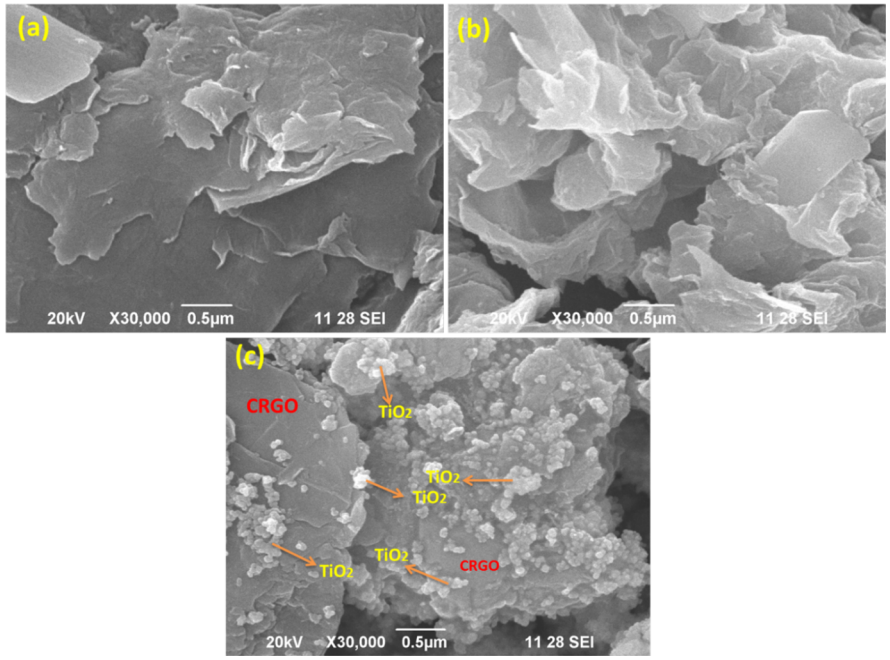

Figure 11. Morphology of GO, GRGO, TiO_2, and GRGO−TiO_2. FE-SEM images of (a) GO, (b) GRGO, and (c) GRGO−TiO_2 (inset therein represents TiO_2).

it showed more intense and sharp peaks at 25.21° (101), 37.77° (004), and 47.94° (200), while the peaks corresponding to the latter that emerged at 27.8° (110) and 35.9° (211) were less intense.[32] In GRGO−TiO_2, the peaks relevant to GRGO and TiO_2 coexisted and confirmed the formation of the hybrid.[33−35] The FTIR spectrum of graphite oxide showed a broad band at 3100 cm^{-1} corresponding to the O−H group and relatively sharp peaks at 1707 and 1514 cm^{-1} indicating the C═O group. The peaks at 1205 and 980 cm^{-1} corresponded to the C−O bond and epoxy group, respectively.[36] TiO_2 nanoparticles show a band at around 673 cm^{-1} attributable to the Ti−O bond and at 3454 cm^{-1}corresponding to the O−H group.[37] The transmittance intensity of graphite oxide peaks was considerably decreased in GRGO due to reduction. So, the peaks relevant to TiO_2 were predominantly observed in the respective GRGO−TiO_2. The Raman spectrum of graphite oxide, GRGO, and GRGO−TiO_2 showed D and G bands at 1365 and 1605 cm^{-1} corresponding to the sp^2 hybridized C−C bonds.[38] The I_D/I_G intensity ratio of GRGO was observed to be 1.15, which is much larger than that of graphite oxides and confirms the formation of GRGO from GO by the reduction. TiO_2 exhibited Raman peaks at 139, 407, 517, and 641 cm^{-1} corresponding to Eg, B_{1g}, A_{1g}, and E_g vibrations of the anatase phase.[39] Like FTIR, XRD and the Raman spectra of GRGO−TiO_2 showed peaks attributable to both TiO_2 (139, 407, 517, and 641 cm^{-1}) and GRGO (1354 and 1601 cm^{-1}) and further confirmed the formation of their hybrid.

3.3. Morphology of GRGO and GRGO−TiO_2. Figures 11a−c and 12a−d show the morphology of graphite oxide, GRGO, TiO_2, and GRGO−TiO_2 hybrids observed with FE-SEM and TEM, respectively. The FE-SEM image (Figure 11a−c) of graphite oxide exhibited a stacked multilayer sheet structure with a very rough surface. Randomly oriented thin sheets were found in the GRGO image. Unlike multilayer sheets, thin sheets possess high surface energy, which favors high disorderliness (entropy) which states that greater the disorder enhance higher entropy, so that the GRGO sheets adopt random orientation. As seen in the inset of Figure 11c, spherical particles with a diameter below 50 nm were formed during hydrothermal synthesis. The surface morphology of GRGO−TiO_2 clearly accounted for the hybrid formation. TiO_2 nanoparticles can be located on the surface and interfaces of the graphene sheet. The surface chemical compositions of these materials were assessed using EDS. The % of oxygen in GO was 12.61; after reduction with SES, it decreased to 1.84, confirming the removal of oxygen functionalities. The % of oxygen and titanium in TiO_2 was 58.87 and 41.13, respectively. The surface of GRGO−TiO_2 was composed of 44.05% oxygen, 44.94% carbon, and 11.01% titanium. The TEM image in Figure 12a−c of GO sheets appeared as few layered. Also, GO sheets were wrinkled and folded. GRGO showed a transparent and single-sheet morphology. The single-sheeted structure indicates the restoration of graphene sheets as a result of the removal of oxygen functionalities during the reduction with SES. The selected area electron diffraction (SAED) patterns are shown as insets. In the SAED pattern, GO exhibits a multiple-ring structure, which is indicative of the multilayered structure, whereas GRGO showed sharp rings corresponding to the short-range ordering of a single-layer graphene sheet.

From the morphological study, GO shows multiple rings in the SAED pattern and a folded wrinkle pattern in the TEM image, indicating the multiple-sheeted patterns present in the GO. From the Raman spectrum has shifted D band to the lower region least to the destruction of the sp^2 character due to the extensive oxidation of graphite sheets, and in the XRD pattern of GO has a higher interlayer spacing of 0.95 nm due to the intercalation of oxygen functionalities such as hydroxyl, epoxy, and carboxyl groups during the oxidation process. After the reduction process, GRGO exhibits the complete removal of the folded and wrinkle pattern in the TEM image, and also, it shows sharp rings in the SAED pattern, indicating the presence of a single-sheeted system, which corresponds to the removal of oxygen-containing functional groups from the GO structure.

https://dx.doi.org/10.1021/acsomega.0c02325
ACS Omega 2021, 6, 14734−14747

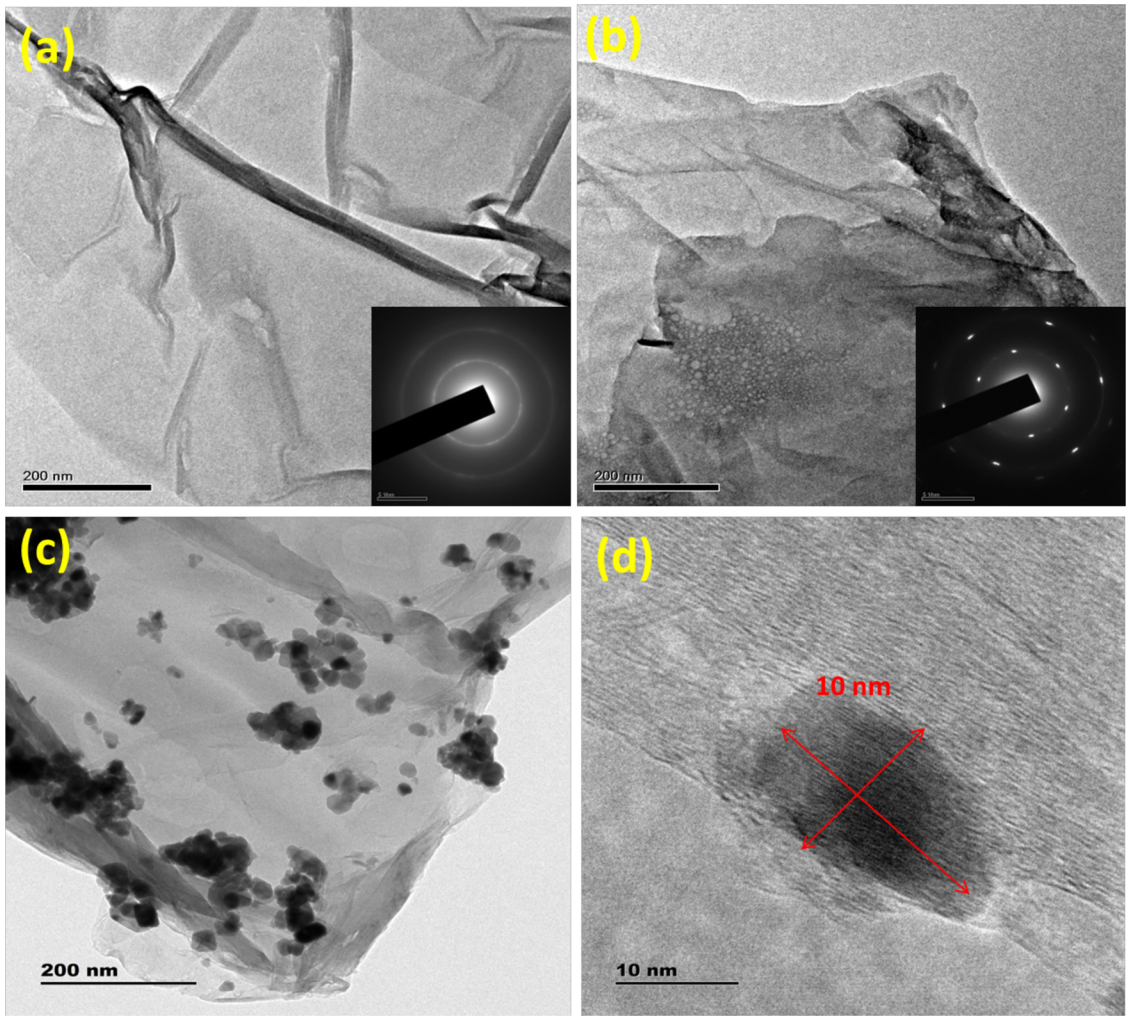

Figure 12. TEM images of (a) GO, (b) GRGO, (c) GRGO−TiO_2, and (d) TiO_2 nanoparticles on GRGO sheet. Insets therein (a and b) represent the respective SAED pattern.

Due to the higher intensity ratio (I_D/I_G) of the D band to the G band in the Raman spectrum with reduction time, responsible for the removal of the oxygen-containing functional groups from GO and in the GRGO exhibits a lower interlayer spacing because of the removal of oxygen-containing functional groups from their structure.

3.4. Electrochemical Properties of GRGO and GRGO−TiO_2 Working Electrodes. The electrochemical behavior of synthesized materials (working electrode) was studied using a three-electrode cell (Ag/AgCl, KCl (reference electrode); Pt wire (counter electrode); and electrode coated with synthesized materials (working electrode)) in 6 mol KOH electrolyte medium. Figure 13a−d shows the CV curves for the working electrode coated with synthesized TiO_2 and graphene materials. These electrodes exhibit quasi-rectangular-shaped curves without redox peaks.[16] When the potential is applied, a fast charging and discharging behavior was observed. Thus, these materials were found to be stable and rechargeable. Figure 14a−d shows the charge−discharge curves. Large enclosed CV curves were obtained for TiO_2, GRGO, and GRGO−TiO_2. The galvanostatic charge−discharge study was used to evaluate the specific capacitance of this electrode material. Potential window was between −0.4 and 0.6 V, and a saturated calomel electrode at 5 mV s^{-1} current density was used.

The specific capacitance values of these prepared electroactive materials were calculated using eq 2:

$$C_S = \frac{I \times \Delta t}{m \Delta V} \tag{2}$$

where I is the discharge current (A), t is the discharge time (s), m is the mass of the loaded electroactive material (g), and v is the operating voltage (V). The specific capacitance values were calculated using eq 1 and are given in Table 1. The specific capacitance of TiO_2, GRGO, and their hybrid was 125, 150, and 175 F g^{-1}, respectively. The GRGO−TiO_2 hybrid exhibited a higher capacitance value due to the high electroactivity of TiO_2 and greater surface area of GRGO. GRGO enhances the availability of electroactive sites, and the layered composite materials enhance the rate of the reaction between the electrode material and ions of the electrolyte, leading to excellent conductivity.

Figure 15a shows the Nyquist plot. The plot gives a semicircle in the higher-frequency region and a short Warburg section between the semicircle and the slope of the line, the straight line of the higher-frequency region that is almost parallel to the imaginary components of the impedance. The semicircle obtained in the high-frequency region on the real axis responds to the charge-transfer resistance. It indicates that the ions of the electroactive materials have good conductivity.

https://dx.doi.org/10.1021/acsomega.0c02325
ACS Omega 2021, 6, 14734−14747

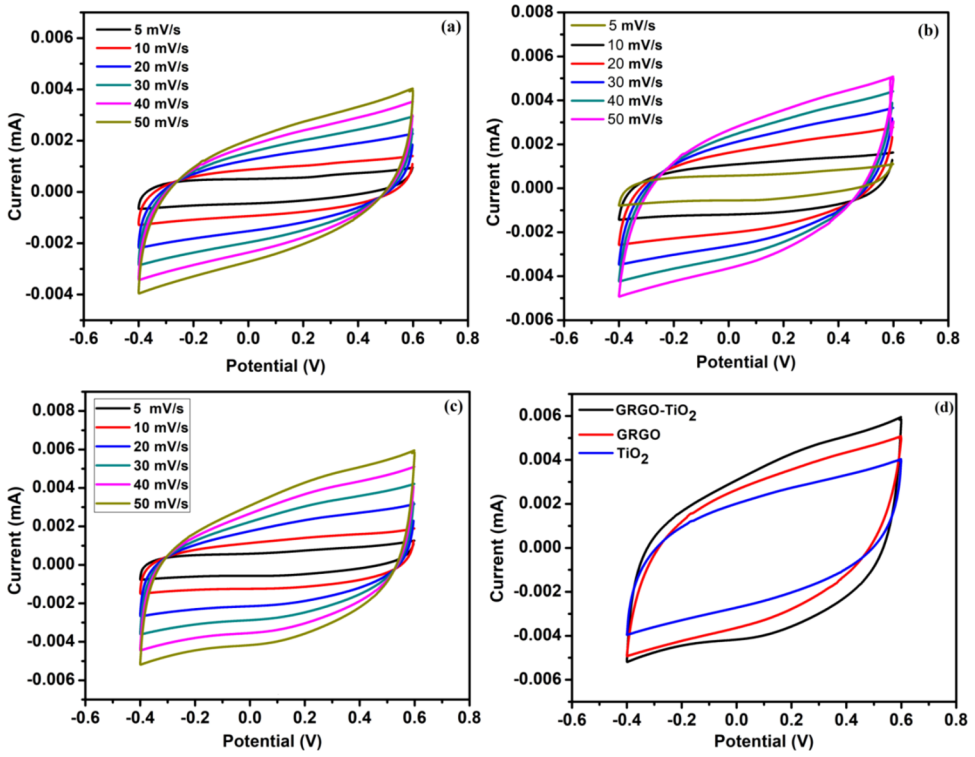

Figure 13. CV curves of (a) TiO_2, (b) GRGO, (c) and GRGO−TiO_2 nanocomposites and (d) overall comparisons of corresponding materials measured in a three-electrode system with 6 M KOH electrolyte.

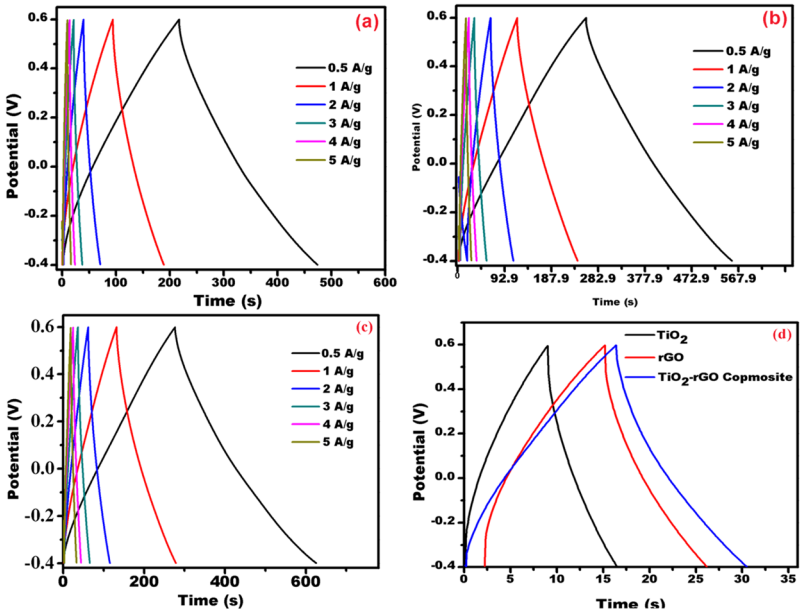

Figure 14. GCD curves of (a) TiO_2, (b) GRGO, and (c) GRGO−TiO_2 composites and (d) overall comparisons of corresponding materials measured in a three-electrode system with 6 M KOH electrolyte.

Table 1. Specific Capacitance of GRGO, TiO_2, and the GRGO−TiO_2 Composite

s. no.	electrode material	current (mA)	specific capacitance (F/g)
1	TiO_2	0.5	125
2	green GRGO	0.5	150
3	green GRGO−TiO_2 composite	0.5	175

The low-frequency region exhibiting a straight line at an angle of 45° shows the ″Warburg resistance″ that depicts the diffusion resistance of the charged ions in the materials and electrodes. The straight line presence in the low-frequency region corresponds to the ideal capacitance behavior of the prepared electrode materials. Notably, the GRGO−TiO_2 hybrid showed better charge-transfer behavior than its constituents alone. The stability and reversibility are important parameters that determine the overall performance of an

https://dx.doi.org/10.1021/acsomega.0c02325
ACS Omega 2021, 6, 14734−14747

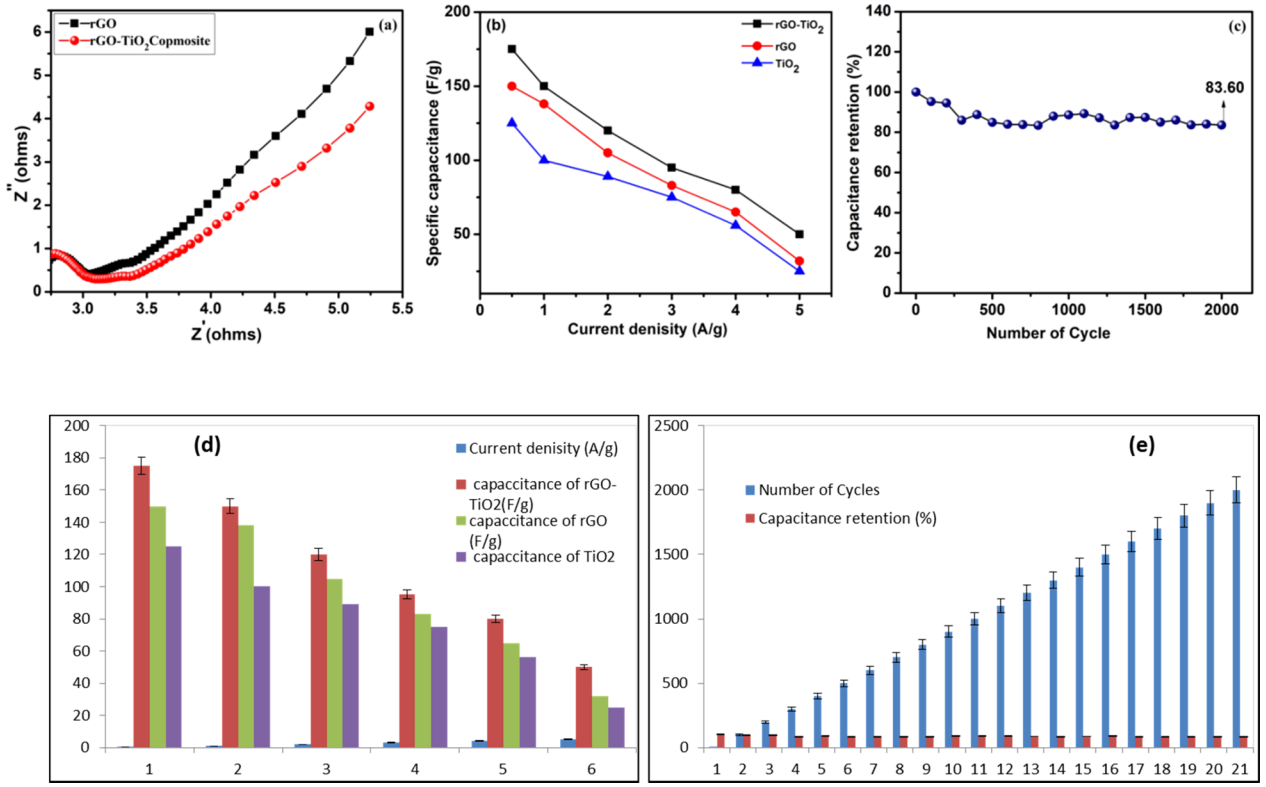

Figure 15. (a) The EIS of GRGO and GRGO−TiO_2 nanocomposites.(b) Plot of specific capacitance of GRGO−TiO_2 nanocomposites versus current density. (c) Capacity retention studies for GRGO/TiO_2 nanocomposite over 2000 charge−discharge cycles. Error bars for the (d) current density and (e) cyclic stability.

electrode material.[40] As shown in Figure 15b, discharging time is decreased as a function of increase in current density due to the complete diffusion of electrolyte ions into the pores of the electrode material at higher current densities.[41] All the prepared electrode materials were subjected to a stability study such as the 1000 cycle experiment in the voltage range of −0.4 to 0.6 V at 5 mV s^{-1} in the CV technique. As the GRGO−TiO_2 hybrid exhibited high performance as an electrode material, it was subjected to the capacitance retention studies as a function of time. For this purpose, the working electrode was subjected to 2000 cycles in the voltage range of −0.4 to 0.6 V and the scanning rate of 5 mVs^{-1}. As shown in Figure 15c, GRGO−TiO_2 exhibits capacitance retention even after 2000 cycles. The developed GRGO−TiO_2 nanocomposite modified electrode shows a better result for supercapacitor application when compared with the reported and published methods by different modified electrodes, and it is shown in Table 2. Figure 15e,f shows the error bar of the current density and cycle stability.

3.5. Photocatalytic Activity. The photocatalytic effect of synthesized GRGO, TiO_2, and GRGO−TiO_2 nanocomposite was carried out in the presence of visible light irradiation. The obtained results are shown in Figure 16a. This figure clearly explains the relationships between irradiation time and rate of decolorization of the BPB dye solution treated by the synthesized materials under visible light irradiation. To compare the catalytic efficiency of the three catalysts, the catalyst dosage was kept constant (20 mg) and the degradation studies were carried out with 1×10^{-5} M BPB dye with varying time intervals. After 60 min of irradiation under visible light, the decolorization rates of the BPB dye solution are 93, 64, and 30% for the GRGO−TiO_2, TiO_2, and GRGO, respectively.

Table 2. Comparison of the Voltammetry Performance with Other Methods for Supercapacitor Application

s. no.	electrode material/ synthesis method	current (mA)	specific capacitance (F/g)	ref.
1	reduced GO (rGO)	0.5	112	42
2	rGO/Zn powder	1	130	43
3	rGO	100 mV/s (scan rate)	136	44
4	rGO/CuO	5 mV/s (scan rate)	137	45
5	TiO_2 decorated reduced graphene oxide composite	0.5	175	present work

The reason for the enhanced photocatalytic activity of GRGO−TiO_2 compared to GRGO and TiO_2 is that GRGO promotes the separation of photogenerated electron holes of titanium oxide. This observation is also reflected in PL results that also support the decreased probability of charge recombination in GRGO−TiO_2. The reason for the inhibition of recombination process in GRGO−TiO_2 is the fact that GRGO acts as a trap for the excitons generated by TiO_2.

3.6. Effect of Catalyst Dosages. To evaluate the effect of catalytic dosages to degrade the BPB dye solution, the photocatalysis experiments were performed by varying the catalyst dosage between 10 and 50 mg of GRGO−TiO_2, while the amount of the BPB solution was kept constant. It can be observed from the degradation plot (Figure 16b) that when the catalyst dose was increased, the percentage degradation also varied. The maximum degradation was observed when the catalyst dosage was 20 mg, beyond which the BPB degradation decreased. The decrease in the photocatalytic oxidation of BPB

https://dx.doi.org/10.1021/acsomega.0c02325
ACS Omega 2021, 6, 14734−14747

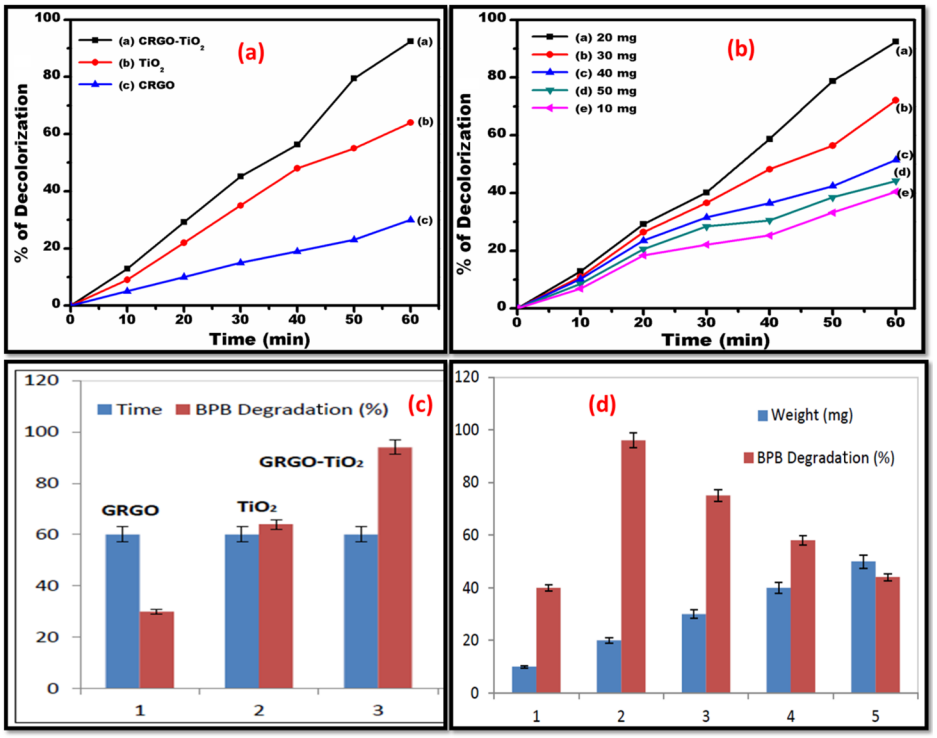

Figure 16. (a) Photocatalytic degradation of bromophenol blue dye (BPB) [1×10^{-5} M, 100 mL] by 20 mg of GRGO, TiO_2, and GRGO−TiO_2. (b) Degradation of the BPB dye as a function of different dosages of GRGO−TiO_2. Error bars for the (c) material and (d) dosage variations.

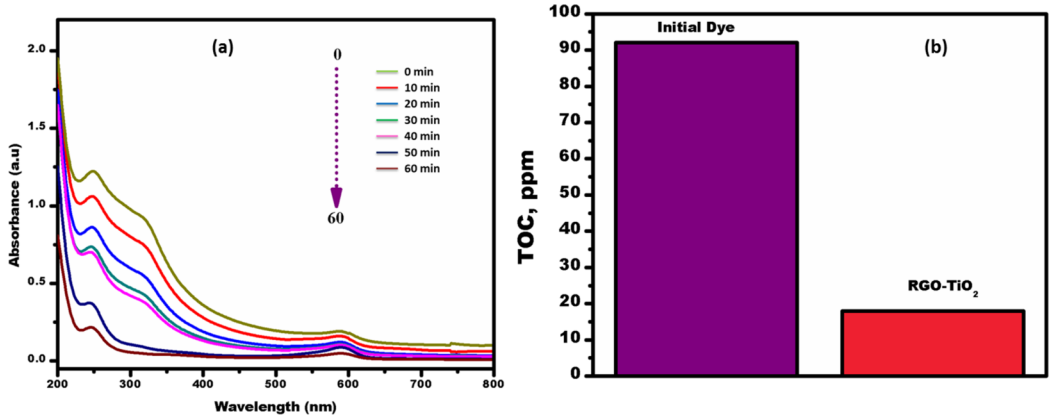

Figure 17. (a) UV−vis spectral changes for the degradation of the BPB dye under visible light irradiation using the GRGO/TiO_2 nanocomposite catalyst. (b) TOC analysis of the BPB dye degradation in the presence of different catalysts under visible light irradiation.

can be attributed to the increased light scattering due to the higher catalyst amount that led to the decreased photon interaction with the catalyst. Figure 16c,d shows the error bar of the material and dosage variation. In addition to this, the agglomeration of the catalyst particles decreased the number of active sites on the catalyst that resulted in decreased degradation beyond the optimum catalyst concentration. The optimum concentration was found to be 200 mg/L with 96% degradation for 60 min of contact time.

3.7. UV−Vis Absorption Spectroscopy. Figure 17a shows the UV−vis absorption spectra of the BPB dye solution at different reaction times. The spectra clearly show the five peaks that are normally observed for the BPB dye solution. The BPB dye shows a chromophore peak at 248 nm that corresponds to the blue color of the BPB dye, and the other three peaks at 590 nm correspond to the benzoic ring structure in the dye molecule. After 60 min of irradiation, the peak intensity of the BPB dye peaks was gradually decreased and finally showed the minimum intensity peak after 60 min of irradiation in the presence of the GRGO−TiO_2 nanocomposite. After the completion of the degradation process, in the visible region, a very small absorption band was seen because of the maximum degradation of the BPB dye by the nanocomposite catalyst, and it clearly confirms the degradation ability of the GRGO−TiO_2 nanocomposite in the photocatalytic process.

3.8. Total Organic Counts (TOCs). A TOC experiment was used to examine the mineralization property of the GRGO−TiO_2 nanocomposite on the BPB dye under visible light irradiation; it is shown in Figure 17b. The TOC of BPB before and after the photocatalysis with GRGO−TiO_2 was found to be 92 and 18 ppm, respectively. The 82% decrease in

https://dx.doi.org/10.1021/acsomega.0c02325
ACS Omega 2021, 6, 14734−14747

TOC after photocatalysis confirms the mineralization of BPB in H_2O and CO_2.

3.9. Plausible Photodegradation Mechanism. The probable mechanism of the catalytic action for GRGO−TiO_2 is schematically represented in Figure 18. Upon irradiation of

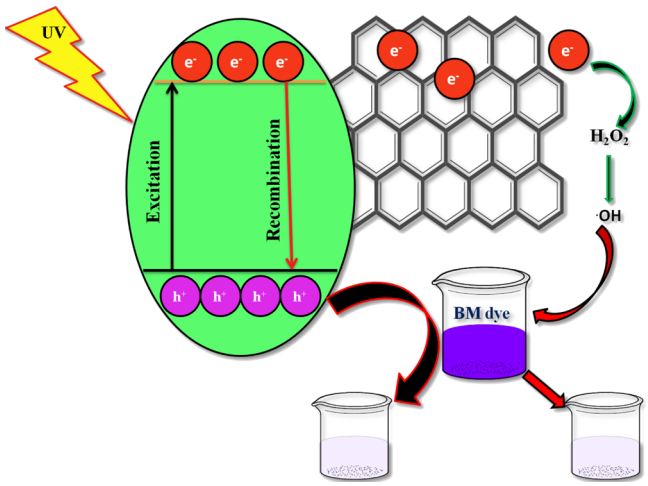

Figure 18. Schematic depicting the mechanism for the degradation of the BPB dye by GRGO−TiO_2.

GRGO−TiO_2 with visible light, the excitons are created due to the promotion of valence electrons to a conduction band and are readily moved to the GRGO surface, and then photogenerated electrons and electron−hole pairs are formed. In the presence of GRGO, the GRGO sheets act as a trap, leading to the inhibition of sudden recombination and delay of the recombination process of the photogenerated electrons into the electron−hole pairs. The trapped electrons in the GRGO react with dissolved oxygen in water molecules, causing the formation of superoxide and hydroxyl free radicals. These reactive species oxidize the BPB molecules. The enhanced oxidation is due to surface adsorption of BPB molecules on to the GRGO surface that makes the availability of pollutants for the reactive species, which leads to the enhanced photooxidation of pollutants. The photogenerated electron−hole pairs on the conduction band also directly react with water molecules and form hydroxyl radicals, which again are involved in the dye molecule degradation mechanism. The GRGO/TiO_2 nanocomposite adsorbed the excess of dye molecules because of this large surface area.

$$TiO_2 + h\upsilon \rightarrow TiO_2(h^+ + e^-) \quad (3)$$

$$GRGO + TiO_2(h^+ + e^-) \rightarrow GRGO(e^- + TiO_2(h^+)) \quad (4)$$

$$TiO_2(e^-) + O_2^- \rightarrow TiO_2 + O_2^{\bullet -} \quad (5)$$

$$GRGO(e^-) \rightarrow CRGO + O_2^{\bullet -} \quad (6)$$

$$TiO_2(h^+) + H_2O \rightarrow TiO_2 + H^+ + OH^{\bullet} \quad (7)$$

$$(TiO_2)e + BPB \rightarrow (TiO_2)e^- + BPB^{+-} \quad (8)$$

$$BPB^{+-} + O_2^- \rightarrow \text{degraded products} + CO_2 + H_2O \quad (9)$$

$$BPB^{+-} + OH^{\bullet} \rightarrow \text{degraded products} + CO_2 + H_2O \quad (10)$$

3.10. Stability and Reusability of the Photocatalyst. Figure 19a shows the efficiency of the GRGO−TiO_2 catalyst upon reuse for six consecutive experiments. After completing each experiment, the used catalyst underwent ultra-centrifugation, the precipitate was filtered, surface active sites were regenerated by acid (such as diluted sulfuric acid) washing followed by DD water washing, and the final dried catalyst powder was obtained. The regenerated catalyst was reused for the further degradation of the fresh BPB model pollutant aqueous solution. From the regeneration and reuse experiments, it was evident that for up to six consecutive experiments, the catalyst retained the efficiency of ∼92%. The small decrease in the percentage degradation of BPB might be due to the surface area and active site losses during the drying process of regeneration. The insignificant decrease in the efficiency of the catalyst confirms the stability of the

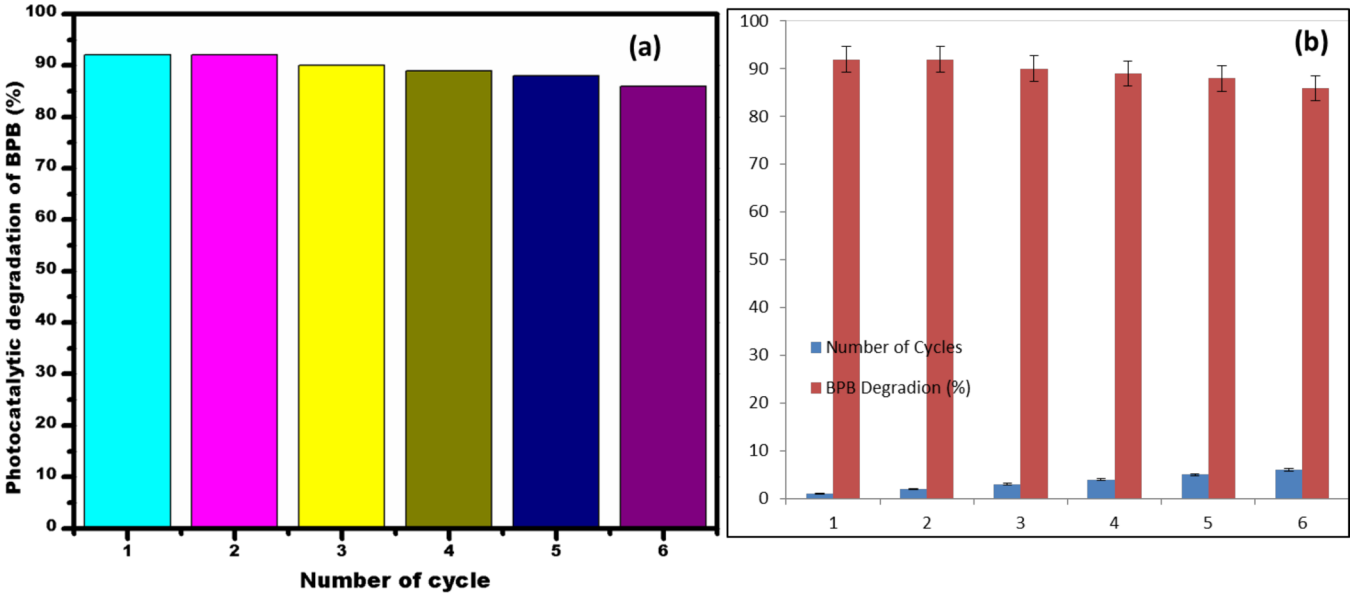

Figure 19. (a) Degradation of the BPB dye for six consecutive times by GRGO−TiO_2. (b) Error bars for the cyclic stability.

https://dx.doi.org/10.1021/acsomega.0c02325
ACS Omega 2021, 6, 14734−14747

catalyst within the number of experiments conducted. Figure 19b shows the error bar of the cycle stability. Figure 19a,b (Figure 20) exhibits the XRD patterns of the GRGO−TiO_2

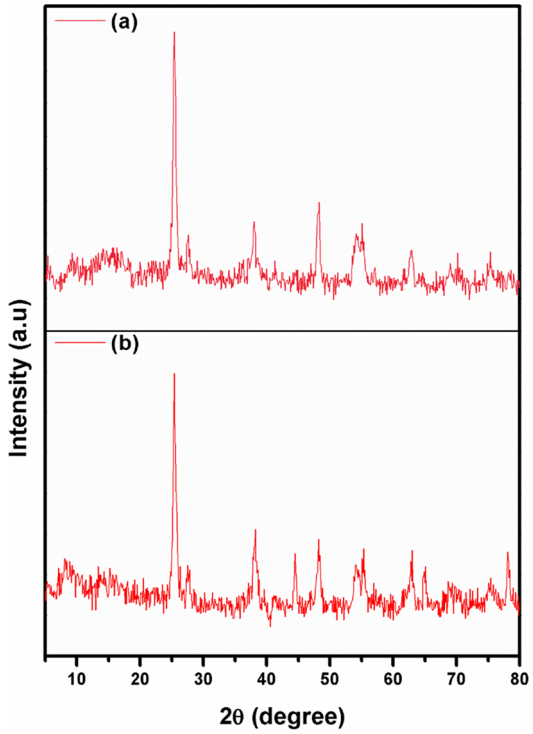

Figure 20. XRD patterns of GRGO−TiO_2 hybrid (a) before the photocatalytic process and (b) after the photocatalytic process.

nanocomposite carried out (a) before and (b) after four cycles. It exhibits the peaks of the unused GRGO−TiO_2 at 25.2, 37.7, and 47.9°, which are similar to the used GRGO−TiO_2 peaks in the study after the photocatalytic process. The XRD patterns exhibit the stable behavior of the GRGO−TiO_2 nanocomposite under photocatalytic study. This experiment result suggests that the GRGO−TiO_2 nanocomposite functions as a photocatalytic study and is suitable for mineralizing a variety of organic dyes.

3.11. Scavenging Effects. The photodegradation effects of the GRGO−TiO_2 nanocomposite on the BPB dye were also confirmed by scavenging studies, which are used to study the reactive species' role in the photocatalytic mechanism (Figure 21). The following scavengers are used to examine the scavenging studies: tetraethylammonium oxalate (TEAO), benzoquinone (BQ), DMSO, and isopropanol (IPA) with active radicals h^+, $O2^{\bullet-}$, e^-, and $^{\bullet}OH$, respectively. For the catalytic performance, this experiment was carried out without scavengers in the same conditions with these four active radicals on the BPB dye in the presence of the GRGO−TiO_2 nanocomposite. After completing the degradation process, the GRGO−TiO_2 nanocomposite shows 93, 45, 65, and 58% MG degradation for the catalyst, AO, BQ, and IP, respectively. Therefore, this experiment confirms the active radical's participation in the photocatalytic mechanism and involvement in the production. The GRGO−TiO_2 nanocomposite shows a better result for photocatalytic application for BPB dye removal when compared with the reported and published methods by different photocatalytic materials, and it is shown in Table 3.

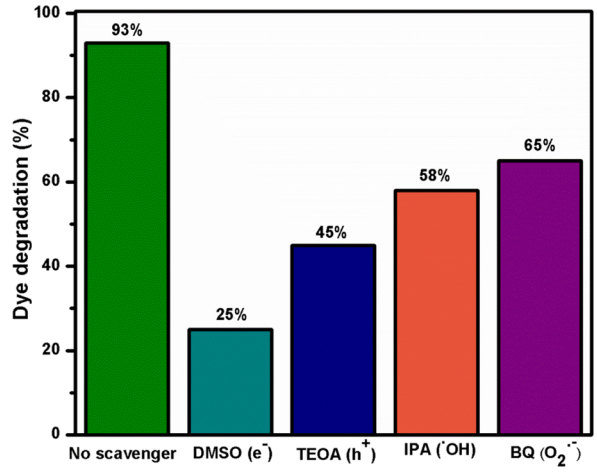

Figure 21. Quenching studies of the GRGO−TiO_2 nanocomposite on MG dye degradation by using different radical scavengers.

Table 3. Comparative Photocatalytic Study of the GRGO−TiO_2 Composite with Other Catalysts for Photocatalyst Application

s. no.	catalysts	% of degradation of BPB dye	ref.
1.	graphene-nanoplates-supported TiO_2	86%	46
2	AgBr−ZnO nanocomposite	89.3%	47
3.	TiO_2 nanoparticles	85.51%	48
4.	ZnO and Ag+ doped ZnO	87%	49
5.	tricobalt tetroxide (Co_3O_4) nanoparticles	89.8%	50
6.	anatase TiO_2 decorated reduced graphene oxide composite	93%	present work

4. CONCLUSIONS

The reducing capability of the aqueous phytoextracts successfully prepared from the skin, seeds, and pulp of grape fruit via digestion, grinding, and soxhlet methods was investigated for the synthesis of RGO. The seed extracts showed a higher reducing capability than the others. More preferably, the soxhlet extract of the seed was highly effective in restoring the all-carbon structure of graphene sheets. The higher phenolic content found in the soxhlet extract of the seed was responsible for its higher reducing capability. The hydrothermal deposition of TiO_2 nanoparticles on the GRGO is confirmed by the presence of peaks relevant to TiO_2 in the FTIR and Raman spectra and XRD of GRGO−TiO_2 hybrids. The SEM and TEM study shows the few-layered structure of GRGO and the presence of TiO_2 nanoparticles in the GRGO−TiO_2 hybrids. The TiO_2 nanoparticles decorated on the GRGO sheets increased the specific capacitance of GRGO−TiO_2 by 25 F g^{-1} with outstanding stability (83.6% of the initial specific capacitance remained after 2000 cycles). In addition, the GRGO−TiO_2 exhibited ∼30% higher photocatalytic efficiency, which is much higher than that of TiO_2. Upon photocatalysis, it was also evident that GRGO−TiO_2 mineralized 92% of the BPB dye and showed stable efficiency over six times of reuse. Finally, this work demonstrates that SES has higher reducing properties than the other extracts for preparing GRGO. Therefore, it can be concluded that SES can be a promising potential eco-friendly reducing agent, which is suitable for synthesis of GRGO−TiO_2 hybrid composite for application as an advanced supercapacitor electrode and

https://dx.doi.org/10.1021/acsomega.0c02325
ACS Omega 2021, 6, 14734−14747

developing a novel photocatalytic material for water purification.

■ ASSOCIATED CONTENT

Supporting Information

The Supporting Information is available free of charge at https://pubs.acs.org/doi/10.1021/acsomega.0c02325.

GC−MS chromatogram of the soxhlet extract of grape seeds (PDF)

■ AUTHOR INFORMATION

Corresponding Author

Samuel Vasanthkumar − *Department of Chemistry, Karunya Institute of Technology and Sciences (KITS), Coimbatore 641-114, Tamil Nadu, India;* orcid.org/0000-0001-9623-6672; Phone: +91 9442429024; Email: kumar2359@yahoo.com

Authors

Subramanian Ramanathan − *Department of Chemistry, Karunya Institute of Technology and Sciences (KITS), Coimbatore 641-114, Tamil Nadu, India*

Sasikumar Moorthy − *Department of Physics, Bishop Heber College (Affiliated to Bharathidasan University), Tiruchirappalli 620017, India;* orcid.org/0000-0003-3191-9450

Subramaniyan Ramasundaram − *Smart Microsystems and Advanced materials Lab (SMALL), School of Mechatronics Engineering, Korea University of Technology and Education, Cheonan, Chungnam 31253, Republic of Korea*

Hari Krishna Rajan − *Department of Chemistry, M.S. Ramaiah Institute of Technology, Bangalore 560054, Karnataka, India;* orcid.org/0000-0003-4939-2781

Sujayakumar Vishwanath − *School of Materials Science and Engineering, Nanyang Technological University, 639798, Singapore;* orcid.org/0000-0002-4526-1453

SteplinPaulSelvin Selvinsimpson − *School of Environmental Science and Engineering, Huazhong University of Science and Technology, Wuhan, Hubei 430074, China*

Arulappan Durairaj − *School of Environmental and Safety Engineering, Jiangsu University, Zhenjiang 212013, PR China*

Byungki Kim − *Smart Microsystems and Advanced materials Lab (SMALL), School of Mechatronics Engineering, Korea University of Technology and Education, Cheonan, Chungnam 31253, Republic of Korea;* orcid.org/0000-0003-0165-4973

Complete contact information is available at: https://pubs.acs.org/10.1021/acsomega.0c02325

Author Contributions

The manuscript was written through the contributions of all authors. All authors have given approval to the final version of the manuscript.

Notes

The authors declare no competing financial interest.

■ ACKNOWLEDGMENTS

S. Ramanatham, A. Durairaj, and S. Vasanthkumar thank the management and administration of Karunya University for their support and help. The authors are grateful to the Department of Science and Technology, Government of India, for its financial support. S. Ramasundaram and B. Kim acknowledge the Korea Ministry of Education, Science, and Technology for its financial support via the National Research Foundation of Korea for the priority Research Centers Program (NRF-2018R1A6A1A03025526) and in part by the Sabbatical Research Promotion Funding from the Korea University of Technology and Education.

■ REFERENCES

(1) Zhu, Y.; Murali, S.; Cai, W.; Li, X.; Suk, J. W.; Potts, J. R.; Ruoff, R. S. Graphene and Graphene Oxide Synthesis, Properties, and Applications. *Adv. Mater.* **2010**, *22*, 3906−3924.

(2) Hummers, W. S., Jr.; Offeman, R. E. Preparation of Graphitic Oxide. *J. Am. Chem. Soc.* **1958**, *80*, 1339−1339.

(3) Marcano, D. C.; Kosynkin, D. V.; Berlin, J. M.; Sinitskii, A.; Sun, Z.; Slesarev, A.; Alemany, L. B.; Lu, W.; Tour, J. M. Improved Synthesis of Graphene Oxide. *ACS Nano* **2010**, *4*, 4806−4814.

(4) Dreyer, D. R.; Park, S.; Bielawski, C. W.; Ruoff, R. S. The chemistry of graphene oxide. *Chem. Soc. Rev.* **2010**, *39*, 228−240.

(5) Tavakoli, F.; Salavati-Niasari, M.; Badiei, A.; Mohandes, F. Green synthesis and characterization of graphene nanosheets. *Mater. Res. Bull.* **2015**, *63*, 51−57.

(6) Teymourinia, H.; Salavati-Niasari, M.; Amiri, O.; Safardoust-Hojaghan, H. Synthesis of graphene quantum dots from corn powder and their application in reduce charge recombination and increase free charge carriers. *J. Mol. Liq.* **2017**, *242*, 447−455.

(7) Khojasteh, H.; Salavati-Niasari, M.; Safajou, H.; Safardoust-Hojaghan, H. Facile reduction of graphene using urea in solid phase and surface modification by N-doped graphene quantum dots for adsorption of organic dyes. *Diamond Relat. Mater.* **2017**, *79*, 133−144.

(8) Yu, Q.; Jauregui, L. A.; Wu, W.; Colby, R.; Tian, J.; Su, Z.; Cao, H.; Liu, Z.; Pandey, D.; Wei, D.; Chung, T. F.; Peng, P.; Guisinger, N. P.; Stach, E. A.; Bao, J.; Pei, S.-S.; Chen, Y. P. Control and characterization of individual grains and grain boundaries in graphene grown by chemical vapour deposition. *Nat. Mater.* **2011**, *10*, 443−449.

(9) Acik, M.; Chabal, Y. J. A Review on Thermal Exfoliation of Graphene Oxide. *J. Mat. Sci. Res.* **2013**, *2*, 101.

(10) Gurunathan, S.; Han, J. W.; Eppakayala, V.; Kim, J.-H. Microbial reduction of graphene oxide by Escherichia coli: a green chemistry approach. *Colloids Surf., B* **2013**, *102*, 772−777.

(11) Chouhan, R. S.; Pandey, A.; Qureshi, A.; Ozguz, V.; Niazi, J. H. Nanomaterial resistant microorganism mediated reduction of graphene oxide. *Colloids Surf., B* **2016**, *146*, 39−46.

(12) Chong, S. W.; Lai, C. W.; Abdul Hamid, S. B. Green preparation of reduced graphene oxide using a natural reducing agent. *Ceram. Int.* **2015**, *41*, 9505.

(13) Nasrollahzadeh, M.; Sajadi, S. M.; Rostami-Vartooni, A.; Alizadeh, M.; Bagherzadeh, M. Green synthesis of the Pd nanoparticles supported on reduced graphene oxide using barberry fruit extract and its application as a recyclable and heterogeneous catalyst for the reduction of nitroarenes. *J. Colloid Interface Sci.* **2016**, *466*, 360−368.

(14) Wang, Y.; Shi, Z. X.; Yin, J. Facile Synthesis of Soluble Graphene via a Green Reduction of Graphene Oxide in Tea Solution and Its Biocomposites. *ACS Appl. Mater. Interfaces* **2011**, *3*, 1127−1133.

(15) Kuila, T.; Bose, S.; Khanra, P.; Mishra, A. K.; Kim, N. H.; Lee, J. H. A green approach for the reduction of graphene oxide by wild carrot root. *Carbon* **2012**, *50*, 914−921.

(16) Thakur, S.; Karak, N. Green reduction of graphene oxide by aqueous phytoextracts. *Carbon* **2012**, *50*, 5331−5339.

(17) Maier, T.; Schieber, A.; Kammerer, D. R.; Carle, R. Residues of grape (Vitis vinifera L.) seed oil production as a valuable source of phenolic antioxidants. *Food Chem.* **2009**, *112*, 551−559.

(18) Shi, J.; Yu, J.; Pohorly, J. E.; Kakuda, Y. Polyphenolics in Grape Seeds-Biochemistry and Functionality. *J. Med. Food* **2003**, *6*, 291−299.

(19) Amarnath, K.; Mathew, N. L.; Nellore, J.; Siddarth, C. R. V.; Kumar, J. Facile synthesis of biocompatible gold nanoparticles from Vites vinefera and its cellular internalization against HBL-100 cells. *Cancer Nanotechnol.* **2011**, *2*, 121−132.
(20) Stoller, M. D.; Park, S.; Zhu, Y.; An, J.; Ruoff, R. S. Graphene-Based Ultracapacitors. *Nano.Lett.* **2008**, *8*, 3498−3502.
(21) Liang, M.; Zhi, L. Graphene-based electrode materials for rechargeable lithium batteries. *J. Mater. Chem.* **2009**, *19*, 5871−5878.
(22) Han, M. Y.; Özyilmaz, B.; Zhang, Y.; Kim, P. Energy Band-Gap Engineering of Graphene Nanoribbons. *Phys. Rev. Lett.* **2007**, *98*, 206805.
(23) Hong, W.; Xu, Y.; Lu, G.; Li, C.; Shi, G. Transparent graphene/PEDOT−PSS composite films as counter electrodes of dye-sensitized solar cells. *Electrochem. Commun.* **2008**, *10*, 1555.
(24) Liu, Q.; Liu, Z.; Zhang, X.; Yang, L.; Zhang, N.; Pan, G.; Yin, S.; Chen, Y.; Wei, J. Polymer Photovoltaic Cells Based on Solution-Processable Graphene and P3HT. *Adv. Funct. Mater.* **2009**, *19*, 894.
(25) Peng, L.; Peng, X.; Liu, B.; Wu, C.; Xie, Y.; Yu, G. Ultrathin Two-Dimensional MnO2/Graphene Hybrid Nanostructures for High-Performance, Flexible Planar Supercapacitors. *Nano Lett.* **2013**, *13*, 2151−2157.
(26) Wang, Y.; Liu, H.; Zhang, M.; Duan, W.; Liu, B. A dual-functional UiO-66/TiO2 composite for water treatment and CO2 capture. *RSC Adv.* **2017**, *7*, 16232−16237.
(27) Bhattacharya, G.; Sas, S.; Wadhwa, S.; Mathur, A.; McLaughlin, J.; Roy, S. S. Aloe vera assisted facile green synthesis of reduced graphene oxide for electrochemical and dye removal applications. *RSC Adv.* **2017**, *7*, 26680−26688.
(28) Masjedi-Arani, M.; Salavati-Niasari, M. Novel synthesis of Zn2GeO4/graphene nanocomposite for enhanced electrochemical hydrogen storage performance. *Int. J. Hydrogen Energy* **2017**, *42*, 17184−17191.
(29) Mohandes, F.; Salavati-Niasari, M. In vitro comparative study of pure hydroxyapatite nanorods and novel polyethylene glycol/graphene oxide/hydroxyapatite nanocomposite. *J. Nanopart. Res.* **2014**, *16*, 2604.
(30) Salehabadi, A.; Salavati-Niasari, M.; Ghiyasiyan-Arani, M. Self-assembly of hydrogen storage materials based multi-walled carbon nanotubes (MWCNTs) and Dy3Fe5O12 (DFO) nanoparticles. *J. Alloys Compd.* **2018**, *745*, 789−797.
(31) Lang, X.; Zhao, J.; Chen, X. Visible-Light-Induced Photoredox Catalysis of Dye-Sensitized Titanium Dioxide: Selective Aerobic Oxidation of Organic Sulfides. *Angew. Chem. Int. Ed.* **2016**, *55*, 4697−4700.
(32) Nasr, M.; Balme, S.; Eid, C.; Habchi, R.; Miele, P.; Bechelany, M. Enhanced Visible-Light Photocatalytic Performance of Electrospun rGO/TiO2 Composite Nanofibers. *J. Phys. Chem. C* **2017**, *121*, 261−269.
(33) Ghafoor, S.; Ata, S.; Mahmood, N.; Arshad, S. N. Photosensitization of TiO2 nanofibers by Ag2S with the synergistic effect of excess surface Ti3+ states for enhanced photocatalytic activity under simulated sunlight. *Sci. Rep.* **2017**, *7*, 255.
(34) Zhang, Y.; Zhang, N.; Tang, Z.-R.; Xu, Y.-J. Improving the photocatalytic performance of graphene−TiO2 nanocomposites via a combined strategy of decreasing defects of graphene and increasing interfacial contact. *Chem. Phys.* **2012**, *14*, 9167.
(35) Safajou, H.; Khojasteh, H.; Salavati-Niasari, M.; Mortazavi-Derazkola, S. Enhanced photocatalytic degradation of dyes over graphene/Pd/TiO2 nanocomposites: TiO2 nanowires versus TiO2 nanoparticles. *J. Colloid Interface Sci.* **2017**, *498*, 423−432.
(36) Arduini, F.; Amine, A.; Moscone Dinia, D.; Palleschi, G. Biosensors for quality and safety control of olive oil: A review. *Anal. Chem.* **2010**, *431*, 688−1702.
(37) Stankovich, S.; Piner, R. D.; Nguyen, S. T.; Ruoff, R. S. Synthesis and exfoliation of isocyanate-treated graphene oxide nanoplatelets. *Carbon* **2006**, *44*, 3342−3347.
(38) Johra, F. T.; Jung, W. G. RGO−TiO 2 −ZnO composites: Synthesis, characterization, and application to photocatalysis. *Appl. Catal. A-Gen.* **20155**, *491*, 52−57.
(39) Stankovich, S.; Dikin, D. A.; Piner, R. D.; Kohlhaas, K. A.; Kleinhammes, A.; Jia, Y.; Wu, Y.; Nguyen, S. T.; Ruoff, R. S. Synthesis of graphene-based nanosheets via chemical reduction of exfoliated graphite oxide. *Carbon* **2007**, *45*, 1558−1565.
(40) Salari, M.; Aboutalebi, S. H.; Konstantinov, K.; Liu, H. K. A highly ordered titania nanotube array as a supercapacitor electrode. *Phys. Chem. Chem. Phys.* **2011**, *13*, 5038.
(41) Zhang, L. L.; Zhou, R.; Zhao, X. S. Graphene-based materials as supercapacitor electrodes. *J. Mater. Chem.* **2010**, *20*, 5983−5992.
(42) Natarajan, S.; Ede, S. R.; Bajaj, H. C.; Kundu, S. Environmental benign synthesis of reduced graphene oxide (rGO) from spent lithium-ion batteries (LIBs) graphite and its application in supercapacitor. *Colloids Surf., A* **2018**, *543*, 98−108.
(43) Li, Y.-F.; Liu, Y.-Z.; Zhang, W.-K.; Guo, C.-Y.; Chen, C.-M. Green synthesis of reduced graphene oxide paper using Zn powder for supercapacitors. *Mater. Lett.* **2015**, *157*, 273−276.
(44) Bo, Z.; Shuai, X.; Mao, S.; Yang, H.; Qian, J.; Chen, J.; Yan, J.; Cen, K. Green preparation of reduced graphene oxide for sensing and energy storage applications. *Sci. Rep.* **2015**, *4*, 4684.
(45) Sudhakar, Y. N.; Hemant, H.; Nitinkumar, S. S.; Poornesh, P.; Selvakumar, M. Green synthesis and electrochemical characterization of rGO−CuO nanocomposites for supercapacitor applications. *Ionics* **2017**, *23*, 1267−1276.
(46) Shah, T.; Gul, T.; Saeed, K. Photodegradation of bromophenol blue in aqueous medium using graphene nanoplates-supported TiO_2. *Appl. Water Sci.* **2019**, *9*, 105.
(47) Abdel-Khalek, A. A.; Mahmoud, S. A.; Zaki, A. H. Visible light assisted photocatalytic degradation of crystal violet, bromophenol blue and eosin Y dyes using AgBr-ZnO nanocomposite. *Environ. Nanotechnol. Monit. Manag.* **2018**, *9*, 164−173.
(48) Dhanalakshmi, J.; Padiyan, D. P. Photocatalytic degradation of methyl orange and bromophenol blue dyes in water using sol−gel synthesized TiO2 nanoparticles. *Mater. Res. Express.* **2017**, *4*, 095020.
(49) Abdel-Khalek, A. A.; Nassar, H. F.; Abdel-Gawad, F. K.; Basem, S. M.; Awad, S. Photocatalytic Degradation of Bromophenol Blue in Wastewater Using Pure ZnO and Ag + Doped ZnO. *Quantum Matter.* **2016**, *5*, 297−304.
(50) Sonkusare, V. N.; Chaudhary, R. G.; Bhusari, G. S.; Mondal, A.; Potbhare, A. K.; Mishra, R. K.; Juneja, H. D.; Abdala, A. A. Mesoporous Octahedron-Shaped Tricobalt Tetroxide Nanoparticles for Photocatalytic Degradation of Toxic Dyes. *ACS Omega* **2020**, *5*, 7823−7835.

https://dx.doi.org/10.1021/acsomega.0c02325
ACS Omega 2021, 6, 14734−14747